Valley- and spin-polarized broken-symmetry states of interacting electrons in gated MoS_2 quantum dots

Ludmiła Szulakowska,[1] Moritz Cygorek,[1] Maciej Bieniek,[1,2] and Paweł Hawrylak[1]
[1]*Department of Physics, University of Ottawa, Ottawa, Ontario, Canada K1N 6N5*
[2]*Department of Theoretical Physics, Wrocław University of Science and Technology, Wybrzeże Wyspiańskiego 27, 50-370 Wrocław, Poland*

(Received 24 June 2020; accepted 4 November 2020; published 9 December 2020)

Understanding strongly interacting electrons enables the design of materials, nanostructures, and devices. Developing this understanding relies on the ability to tune and control electron-electron interactions by, e.g., confining electrons to atomically thin layers of two-dimensional crystals with reduced screening. The interplay of strong interactions on a hexagonal lattice with two nonequivalent valleys, topological moments, and the Ising-like spin-orbit interaction gives rise to a variety of phases of matter corresponding to valley and spin-polarized broken-symmetry states. In this paper we describe a highly tunable strongly interacting system of electrons laterally confined to monolayer transition-metal dichalcogenide MoS_2 by metallic gates. We predict the existence of valley- and spin-polarized broken-symmetry states tunable by the parabolic confining potential using exact diagonalization techniques for up to $N = 6$ electrons. We find that the ground state is formed by one of two phases, both spin and valley polarized or valley unpolarized but spin intervalley antiferromagnetic, which compete as a function of electronic shell spacing. This finding can be traced back to the combined effect of Ising-like spin-orbit coupling and weak intervalley exchange interaction. These results provide an explanation for interaction-driven symmetry-breaking effects in valley systems and highlight the important role of electron-electron interactions for designing valleytronic devices.

DOI: 10.1103/PhysRevB.102.245410

I. INTRODUCTION

The role of electron-electron interactions in determining the many-electron ground and excited states in different materials is controlled by the ratio of Coulomb energy V to kinetic energy T as $V/T = r_s$ where $\pi {r_s}^2$ is an area per electron [1]. For small r_s electrons in two dimensions (2D) are well described by the Fermi-liquid theory but as r_s increases, density decreases, and the spin-polarized and Wigner crystal phases follow [2,3]. In the 2D Hubbard model the electronic phases are controlled by the ratio of on-site Coulomb energy to the tunneling matrix element U/t. On a hexagonal lattice, calculations predict a semimetallic phase followed by the antiferromagnetic and Mott-insulating phase [4–6]. The U/t can be tuned by controlling screening (U) or controlling t. Recent work showed that t can be significantly reduced by twisting layers in bilayer graphene (BG) [7]. The quenching of tunneling results in strongly correlated system with Mott-insulating and superconducting phases [8,9]. Recent experiments in BG [10,11] and transition-metal dichalcogenides (TMDCs) point to potential existence of spin- [12] and valley-polarized (SVP) [13] interaction-driven broken-symmetry valley- and spin-polarized states.

In this paper we focus on a new emerging highly tunable strongly interacting system of N electrons laterally confined to monolayer 2D crystal, such as MoS_2, [14–20] by metallic gates [21–35]. The confinement to a single atomic layer leads to reduced screening and enhanced electron-electron interactions manifested in large ∼300-meV exciton binding energies [16,33,36–38]. Metallic gates can be used to define quantum dots (QDs) with discrete levels with spacings ω and enable a controlled charging of the QDs with N electrons. The ratio V/T scales with ω as $V/T = 1/\sqrt{\omega}$. In small GaAs QDs at large ω, the ground state (GS) is well approximated by configurations minimizing single-particle (SP) energy [39], but in large QDs, for small ω, spin-polarized [39–41] and correlated phases emerge [39,42]. Here we combine the atomistic multimillion atom description of SP states, lateral confining potential and realistic electron-electron interaction matrix elements with accurate exact diagonalization techniques involving up to 5×10^7 configurations to determine GS and excited states of electrons in MoS_2 QDs. We predict valley- and spin-polarized ground states as well as intervalley antiferromagnetic ground states of up to $N = 6$ electrons, dependent on the magnitude of ω.

The paper is organized as follows. Section II presents the tight-binding model of a rectangular computational box of MoS_2 in the atomic site and Bloch state basis and includes the details of the configuration interaction methodology with Keldysh screening used to obtain many-electron states of MoS_2 QDs. In Sec. III we present the results on many electron GS and excited states. Subsection III A discusses the two-electron behavior and the role of spin-orbit coupling as well as the effect of filling of multiple harmonic-oscillator shells. Subsection III B includes the results on many-electron broken-symmetry states for up to $N = 6$ electrons and predictions on experimental signatures of these states. Section IV contains conclusions and plans for future work.

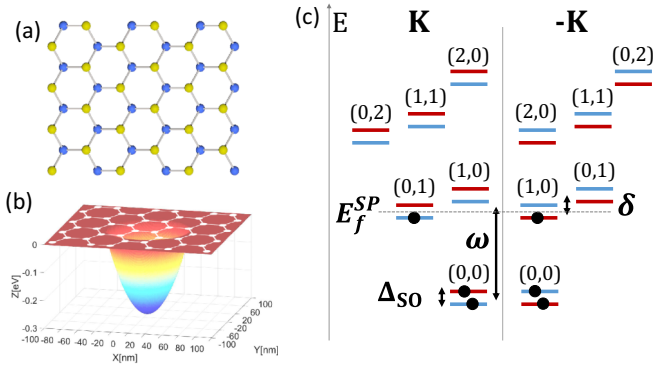

FIG. 1. (a) Rectangular computation box of monolayer MoS_2. Blue (yellow) atoms denote Mo (S) atoms. (b) Example of a parabolic confining potential from the metallic gates (depth of 300 meV). White lattice represents the computation box in which electrons are confined to form a QD. (c) SP energy structure of a MoS_2 QD. The HO shells are doubly degenerate due to valleys K and $-K$. ω denotes shell spacing. Indices (n, m) label HO states. Spin-down and spin-up energy levels are split by the spin-orbit splitting Δ_{SO}, opposite in opposite valleys. HO shells are split by δ due to valley topological moments. To obtain a half-filling for two HO shells $N = 6$ electrons are needed. E_F^{SP} denotes the Fermi level for a noninteracting system of $N = 6$ electrons.

II. MODEL

Figure 1(a) shows the top view of a monolayer MoS_2 lattice. The blue (yellow) atoms correspond to Mo (S) atoms with $3d$ orbitals ($3p$ orbitals) included in the SP Hamiltonian, following Ref. [34],

$$\hat{H}^{TB} = \sum_{i\sigma} E_{i\sigma} c_{i\sigma}^{\dagger} c_{i\sigma} + \sum_{\langle i,j\rangle,\sigma} (T_{ij} c_{i\sigma}^{\dagger} c_{j\sigma} + \text{H.c.}) + \sum_{\langle\langle i,j\rangle\rangle,\sigma} (W_{ij} c_{i\sigma}^{\dagger} c_{j\sigma} + \text{H.c.}), \quad (1)$$

where $c_{i\sigma}^{\dagger}$ creates an electron on state $i\sigma$ (σ is the spin), and i carries an atom unit-cell index, orbital index, and sublattice index. $E_{i\sigma}$ are on-site energies and $T(W)$ are 6×6 nearest-neighbor (NN) (next nearest-neighbor (NNN)) hopping matrices between sites. Energies $E_{i\sigma}$ include the parabolic potential V_i generated by the gates [as shown in Fig. 1(b)] on a site corresponding to index i with $V_i = V(\boldsymbol{r}_i) = |V_{\max}| r_i^2/(R_{QD}^2) - V_{\max}$ for $|\boldsymbol{r}_i| \leqslant R_{QD}$ and 0 elsewhere. $V_{\max}$ is the depth of the potential and R_{QD} is the radius of the QD. The confining potential mixes the conduction band (CB) states, lowers their energy into the energy gap of MoS_2 and confines electrons to the center of a QD.

To avoid edge states in the energy gap we apply periodic boundary conditions, i.e., we wrap the finite computational box with $\sim 10^6$ atoms on a torus with periodic boundary conditions. The Hamiltonian in Eq. (1) can now be written in the basis of Bloch states as

$$\hat{H}_{\boldsymbol{k}\,\text{basis}}^{TB} = \sum_{\boldsymbol{k}} \sum_{\alpha\sigma} E_{\alpha} a_{\boldsymbol{k}\alpha\sigma}^{\dagger} a_{\boldsymbol{k}\alpha\sigma} + \sum_{\boldsymbol{k}\sigma} \sum_{\langle\alpha,\beta\rangle} (e^{i\boldsymbol{k}\boldsymbol{d}_{\alpha,\beta}} T_{\alpha,\beta} a_{\boldsymbol{k}\alpha\sigma}^{\dagger} a_{\boldsymbol{k}\beta\sigma} + \text{H.c.}) + \sum_{\boldsymbol{k}\sigma} \sum_{\langle\langle\alpha,\beta\rangle\rangle} (e^{i\boldsymbol{k}\boldsymbol{d}_{\alpha,\beta}} W_{\alpha,\beta} a_{\boldsymbol{k}\alpha\sigma}^{\dagger} a_{\boldsymbol{k}\beta\sigma} + \text{H.c.}) + \sum_{\boldsymbol{k},\boldsymbol{k}'} \sum_{\boldsymbol{R},\alpha\sigma} (e^{i(\boldsymbol{k}-\boldsymbol{k}')\boldsymbol{R}} V_{\boldsymbol{R},\alpha} a_{\boldsymbol{k}\alpha\sigma}^{\dagger} a_{\boldsymbol{k}'\alpha\sigma} + \text{H.c.}), \quad (2)$$

where $\boldsymbol{R}$ is position of a cell and α carries the orbital and sublattice indices. $\boldsymbol{d}_{\alpha,\beta}$ is the NN or NNN vector between NN or NNN orbitals α, β, and only the confining potential $V_{\boldsymbol{R}\alpha}$ mixes the $\boldsymbol{k}$ states [22].

We diagonalize Eq. (2) to obtain valley-specific QD states. A schematic of a typical low-energy SP spectrum of a QD is presented in Fig. 1(c). It is doubly degenerate due to the valley index $+K$, $-K$. The spectrum for each valley resembles a 2D harmonic-oscillator (HO) ladder with shells separated by the spacing ω, tuned by the depth of the confining potential or QD radius [40,43]. A separate sixfold degenerate HO-like spectrum originating from Q points is present at higher energies (not shown), although it is not occupied by electrons for the range of ω considered here. The SP levels are labeled with p, σ, where $p = [(n, m), K]$ contains state index (n, m) (HO quantum numbers, $n + m$ determines the shell index, and $L = n - m$ is the angular momentum) and valley index $+K$, $-K$, and σ denotes spin. The spin-orbit induced Zeeman splitting Δ_{SO} between spins [$\uparrow$ and $\downarrow$ shown in red and blue, respectively, in Fig. 1(c)] is opposite for both valleys.

A further modification of a simple HO ladder is a topological splitting δ proportional to ω, exhibited by all electronic shells. This splitting arises from the valley topological moments and results in opposite angular momentum L for the lowest-energy states in $+K$ and $-K$ valleys.

We next turn to filling the SP spectrum with electrons up to the Fermi-level E_f^{SP} as illustrated in Fig. 1(c) for $N = 6$ electrons. Our goal is to understand the many-body GS and excited states of interacting electrons and explain how the interactions mix many configurations in forming correlated electronic states.

The many-body Hamiltonian in the basis of SP QD states reads

$$H = \sum_{p\sigma} e_{p\sigma} c_{p\sigma}^{\dagger} c_{p\sigma} + \frac{\eta}{2} \sum_{pqst\sigma\sigma'} \langle pq|V|st\rangle c_{p\sigma}^{\dagger} c_{q\sigma'}^{\dagger} c_{s\sigma'} c_{t\sigma}, \quad (3)$$

where $e_{p\sigma}$ are SP HO states p, σ shown in Fig. 1(c) and the second term includes Coulomb scattering between these states, with η controlling the strength of the interactions. We express the Coulomb matrix elements $\langle pq|V|st\rangle$ in Eq. (3) in the basis of atomic orbitals as $\langle pq|V|st\rangle = \sum_{ijkl} A_i^{p*} A_j^{q*} A_k^{s} A_l^{t} \langle ij|V|kl\rangle$, where A are solutions to the SP Hamiltonian in Eqs. (1) and (2). We include only on-site short-range integrals $\langle ii|V|ii\rangle$, and the long-range part is taken as a classical Coulomb term. The Coulomb integrals are calculated using the Coulomb potential with Keldysh screening [44,45] in order to model realistic Coulomb interaction of charges in 2D materials. The Keldysh screening using the 2D Fourier transform is written as [38]

$$V_K^{3D}(\boldsymbol{r} - \boldsymbol{r}') = \frac{1}{\epsilon^*} \frac{e^2}{4\pi\epsilon_0} \frac{1}{(2\pi)^2} \int_{-\infty}^{\infty} \frac{2\pi}{|\boldsymbol{k}|} \frac{1}{1 + 2\pi\alpha|\boldsymbol{k}|} e^{-|z-z'||\boldsymbol{k}|} \times e^{i\boldsymbol{k}(\boldsymbol{\rho}-\boldsymbol{\rho}')} d^2\boldsymbol{k}, \quad (4)$$

where $\alpha = 2.2$ Å is the 2D polarizability and we take $\epsilon^* = 2.5 = \frac{\epsilon_1+\epsilon_3}{2}$, where $\epsilon_1 = 1.0$ and $\epsilon_3 = 4.0$ are the dielectric constants of the material layers below and above MoS_2, taken here as SiO_2 and vacuum, respectively [46]. All results in the following sections include Keldysh screening of Coulomb interaction.

The N-electron configurations are constructed as $|x\rangle = \prod_{p,\sigma} {c_{p\sigma}}^\dagger|0\rangle$, and the wave function of the N-electron system is expanded in all possible electronic configurations $|x\rangle$. The Hamiltonian matrix in the space of configurations $|x\rangle$ is constructed and diagonalized giving exact eigenstates. E.g., for $N = 6$ we find up to $\sim 5 \times 10^7$ configurations for $M = 60$ SP orbitals, where M is the number of SP orbitals included.

We now turn to discuss the properties of N-electron systems. We focus on $N = 2, 4, 6$ electrons because in a noninteracting system filling (half-filling) the first s shell requires $N = 4$ ($N = 2$) electrons and half-filling of the first two shells is realized with $N = 6$ electrons.

III. RESULTS

A. $N = 2$ electron complex

In order to build the understanding of the role of interactions in MoS_2 QDs, it is instructive to first focus on $N = 2$ electrons on the first fourfold degenerate SP s shell. With no SO splitting Δ_{SO}, this system describes the half-filled lowest-energy shell of BG QD [21,32,35] or a half-filled p shell of a self-assembled QD [39]. The GS is determined by the exchange interaction and can be understood in terms of spin singlets and triplets.

With $N = 2$ electrons on s-shell orbitals in opposite valleys the $N = 2$ electron spin states can be classified into three spin triplets $|T^s_+\rangle = |\uparrow\rangle|\uparrow\rangle$, $|T^s_0\rangle = \frac{1}{\sqrt{2}}(|\uparrow\rangle|\downarrow\rangle + |\downarrow\rangle|\uparrow\rangle)$ or $|T^s_-\rangle = |\downarrow\rangle|\downarrow\rangle$. The total wave function is, therefore, simultaneously a valley singlet $|S^v\rangle = \frac{1}{\sqrt{2}}(|K\rangle|-K\rangle - |-K\rangle|K\rangle)$. The spin triplet valley singlet state $|S^v\rangle|T^s_-\rangle$ is shown schematically in Fig. 2 A. In the absence of Δ_{SO}, the energy of the spin triplet configuration E_T is composed of the sum of SP energies of s-type (0,0) orbitals, the direct interaction V^0_D and intervalley exchange $V^0_X(+K,-K)$ to give $E_T = e_{00,\uparrow} + e_{00,\downarrow} + V^0_D(+K,-K) - V^0_X(+K,-K)$.

The interaction elements as a function of ω have been shown in Fig. 3. The exchange interaction lowers the energy of $|T^s\rangle$ compared to $|S^s\rangle$. Exact diagonalization of the $N = 2$ electron system on the lowest s shell with $\Delta_{SO} = 0$ gives $|S^v\rangle|T^s\rangle$ as the triply degenerate GS due to the intervalley exchange $V^0_X(+K,-K)$. This is in accordance with what has been found for the half-filled p shells of QDs [47] and for BG QDs [32], a two-valley system with negligible SO.

In TMDCs the Ising-like SO interaction leads to spin splitting in the CB ranging from ~3 meV in Mo-based to ~30 meV in W-based material [13,17]. Turning on Δ_{SO} decreases the energy of spin-down states in valley K as well as of spin-up states in valley $-K$. For $N = 2$ electrons this means that the spin triplets $|T^s\rangle$ and spin singlets $|S^s\rangle$ mix and the threefold degeneracy of the $|S^v\rangle|T^s\rangle$ GS is broken by the Δ_{SO}. The splitting Δ_{SO} competes with intervalley exchange $V^0_X(+K,-K)$ (black squares in Fig. 3 right). For such weak intervalley exchange $V^0_X(+K,-K) \ll \Delta_{SO}$ the spin-unpolarized state, depicted as configuration B in Fig. 2, becomes the lower-energy state separated by a gap from the spin-polarized states, configuration A in Fig. 2. This is shown in Fig. 2 (right) for $\omega = 36$ meV and varied η. Configuration B can be written as a mixture of $|S^v\rangle|T^s_0\rangle$ and $|T^v_0\rangle|S^s\rangle$ and becomes the spin-valley singlet $|S^{sv}\rangle = \frac{1}{\sqrt{2}}(|S^v\rangle|T^s_0\rangle - |T^v_0\rangle|S^s\rangle) = \frac{1}{\sqrt{2}}(|K\downarrow\rangle|-K\uparrow\rangle - |-K\uparrow\rangle|K\downarrow\rangle)$.

We now lower the level spacing ω and allow the second shell of p-type SP states to be occupied by a second electron,

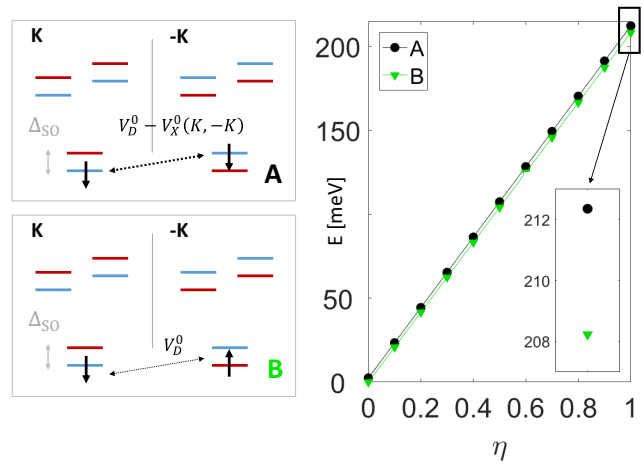

FIG. 2. Configurations A (spin polarized) and B (spin unpolarized) of $N = 2$ electrons in the s shell are valley unpolarized. Electrons in A interact with direct interaction V^0_D and intervalley exchange $V^0_X(K,-K)$ (both include Keldysh screening) but have a higher SP energy due to SO splitting Δ_{SO}. The electrons in B interact only with V^0_D. The right panel shows the energies of A and B for increasing strength of interaction η. Due to much smaller intervalley exchange compared to SO splitting $V^0_X(K,-K) \ll \Delta_{SO}$, B has always lower energy. B makes up the many-body GS for $N = 2$ electrons in one shell, which is valley and spin unpolarized.

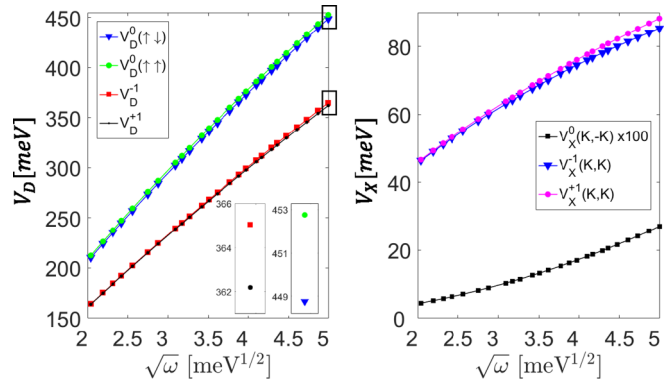

FIG. 3. Coulomb matrix elements determining the GS of $N = 2$ electrons in two HO shells. (Left) Direct Coulomb matrix elements with Keldysh screening and (right) exchange Coulomb matrix elements with Keldysh screening. The direct interaction of electrons on (0,0) and $(1,0)$ $(L = +1)$ is the lowest (black dots on the left), and they interact through the highest exchange (magenta dots on the right).

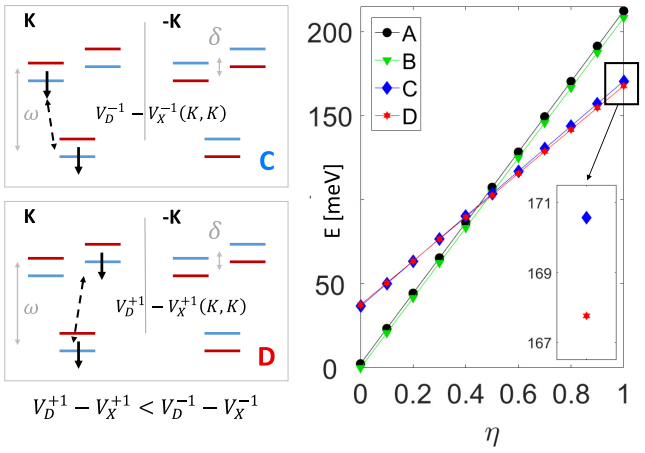

FIG. 4. Configurations A and D of $N = 2$ electrons are both spin polarized with no valley polarization in A and full valley polarization in D. The electrons in (a) interact with intervalley exchange $V_X^0(+K,-K)$, whereas the electrons in D interact with much stronger intravalley exchange $V_X^{+1}(K,K)$, which compensates the SP energy cost ω. This competition generates a transition (right panel) as a function of η. For a noninteracting case at $\eta = 0$, A is lower in energy, but for an interacting system, D has lower energy.

e.g., as shown in Figs. 4 C and 4D. The transfer from the s shell to the p shell costs SP energy $\omega + \delta/2$, but it is compensated by gain in interaction energy. Instead of $V_D^0(+K,-K) - V_X^0(+K,-K)$ for configuration A, the interaction is now $V_D^1(+K,+K) - V_X^1(+K,+K)$ (the superscript denotes L of the second electron). This change lowers the energy of D compared to A and B. This is because of the significantly stronger intravalley exchange $V_X^1(+K,+K)$ compared to intervalley $V_X^0(+K,-K)$ (Fig. 3 right). There are two possible p-shell orbitals and two possible $N = 2$ electron configurations, out of which D [with the second electron in $L = +1$ ($L = -1$) orbital at $+K$ ($-K$)] is always lower in energy. It is clear if one compares the direct and exchange interaction elements: $V_D^1(+K,+K) < V_D^{-1}(+K,+K)$ and $V_X^1(+K,+K) > V_X^{-1}(+K,+K)$ (see Fig. 3).

This competition between configurations A and C and D is shown for $\omega = 36$ meV in Fig. 4 (right). For a noninteracting system, at $\eta = 0$, the valley- and spin-polarized configurations C and D with one electron on a p shell have higher energy compared to valley-unpolarized configuration A. However, as strength of interactions η is increased for Keldysh screened Coulomb interactions, a transition is present and the valley-spin-polarized configuration D moves to the lowest energy. This transition can also be understood by considering the $N = 2$ electron wave function. Configuration D is a product of spin triplet $|T_-^s\rangle$, valley triplet $|T_-^v\rangle$, and, hence, electronic orbital s-p singlet $|S^e\rangle$, written as $|D\rangle = |S^e\rangle|T_-^{sv}\rangle$, where $|T_-^{sv}\rangle = |T_-^v\rangle|T_-^s\rangle$ (corresponding $|T_+^{sv}\rangle$ is degenerate). All other spin, valley, and electronic orbital configurations can be constructed in a similar way, taking into account the nonzero Δ_{SO}. For higher shells D-like configurations $|T_-^{sv}\rangle$ (valley-spin polarized) compete for the GS with the triplet configurations $|T_0^{sv}\rangle$ (valley-spin unpolarized).

B. GS and excited states of $N \geqslant 2$ and $M = 60$

We have so far identified different possible phases of the $N = 2$ electron system and different interactions competing to produce the GS and excited states: SP energies, SO splitting, topological moments, and direct and exchange intravalley and intervalley interactions. We now describe results of exact diagonalization of the $N = 2$–6 electron problem as a function of ω for a varying number of electronic shells. Converged results for five shells per valley ($M = 60$ SP states) for $N = 2$ and $N = 6$ electrons are discussed below. All our numerical results show spin-valley locking in the many-body GS with spin $\uparrow$ ($\downarrow$) electrons occupying valley $+K$ ($-K$) so that $N_\downarrow = N_K$ and $N_\uparrow = N_{-K}$, which is in line with our explanation of the GS of the ($N = 2$)-electron system. This allows us to label the GS with one polarization quantum number $\widetilde{V} = \frac{N_K - N_{-K}}{N}$, denoting total valley polarization and equal here to the total spin-polarization $\widetilde{V} = S_z \frac{2}{N} = \frac{N_\uparrow - N_\downarrow}{N}$.

The results for valley- and spin-polarizations $\widetilde{V}$ for $N = 2$ and $N = 6$ electrons are shown in the top panel of Fig. 4 whereas the corresponding energy gaps $\Delta E_{X-GS} = E_X - E_{GS}$ where E_X is the first excited state and schematic electron configurations are shown in the lower panel.

The colors in Fig. 4 (top) denote the degree of polarization $\widetilde{V}$: orange depicts full SVP with total $|S_z| = N/2$, whereas dark green identifies a fully intervalley antiferromagnetic (IVAF) GS with total $S_z = 0$ ($N_\uparrow = N_\downarrow$) and no net valley polarization ($N_K = N_{-K}$). Schematics corresponding to IVAF and SVP phases are shown for both N's. Clear phase transitions from the IVAF GS to the SVP GS accompanying the closure of energy gaps ΔE_{X-GS} at critical energy spacings $\omega_C \approx 9$ and $\omega_C \approx 8$ meV are visible for $N = 2$ and $N = 6$ electrons, respectively. For $N = 2$, the phases IVAF and SVP correspond to the competing triplets $|T_0^{sv}\rangle$ and $|T_\pm^{sv}\rangle$, respectively.

In the insets of Fig. 5. we show a schematic of the two competing GS phases for $N = 2$ and $N = 6$ electrons with spin $\uparrow$ ($\downarrow$) electrons shown with red up (blue down) arrows. IVAF (left) involves $N_\uparrow = N_{-K} = N_\downarrow = N_K = 1$ and $N_\uparrow = N_{-K} = N_\downarrow = N_K = 3$ for $N = 2$ and $N = 6$, respectively. The SVP phase (right) is fully polarized with $N = N_\downarrow = N_K = 2$ (and a degenerate time-reversed state with $N = N_\uparrow = N_{-K} = 2$) and similarly $N = N_\downarrow = N_K = 6$ (and a degenerate time-reversed state with $N = N_\uparrow = N_{-K} = 6$).

In order to detect the competing GS phases in an experiment, one needs to consider the stability of these phases. It is partly determined by the energy spacing between the GS and the excited state ΔE_{X-GS}, which, in turn, impacts transport measurement. Closing of the energy gaps due to phase transitions would affect the temperature dependence and high-source-drain Coulomb diamonds in transport [48]. The computed energy gaps ΔE_{X-GS} as a function of ω for $N = 2$ (black) and $N = 6$ (red) reach several meV. The quantum phase transitions between IVAF and SVP phases occur when $\Delta E_{X-GS} = 0$.

The predicted here nature of the ground state, either SVP or IVAF for the N-electron system will affect charging

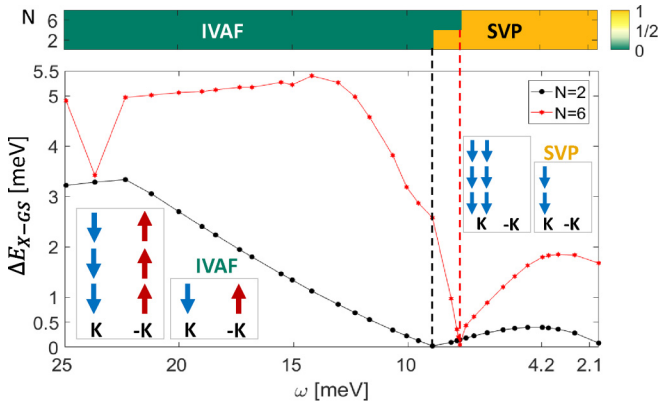

FIG. 5. Top: nature of the GS for $N = 2$ and $N = 6$ electrons for varying ω. Colors depict the polarization quantum number $\widetilde{V}$ (see the text for details): IVAF GS (dark green) and SVP GS (orange). Bottom: the energy difference ΔE_{X-GS} between the GS and the first excited state for varying ω for $N = 2$ (black dots) and $N = 6$ (red stars). Vanishing ΔE_{X-GS} marks a transition in the nature of the GS from the IVAF to the SVP phase (shown with dashed lines). The insets give a schematic of the IVAF and the SVP GS phases (red and blue arrows depict spin up and down).

energies obtained from Coulomb and spin blockade spectroscopies. Excited states shown in Fig. 5 could be obtained from Coulomb diamonds in high source-drain spectroscopy. The predicted gate-induced phase transition in QD would result in temperature dependence of the CB spectra as the energy gap collapses [48].

IV. CONCLUSIONS

Using atomistic theory combined with exact many-body diagonalization tools we predict the existence of broken-symmetry SVP and IVAF electronic states of interacting electrons electrostatically confined in a parabolic QD in a single layer of MoS_2. These results highlight the important role of electron-electron interactions for designing valleytronic devices. We predict that SVP and IVAF states can be probed experimentally in a Coulomb and spin blockade spectroscopy. Large energy gaps between the many-electron GS and excited states suggest stability of these phases and the potential for observing the SVP and IVAF states in transport experiments. Future work will relate these phases with simulation of transport measurements and results of intra- and interband spectroscopies.

ACKNOWLEDGMENTS

L.S., M.C., M.B., and P.H. thank M. Korkusinski, Y. Saleem, A. Altintas, A. Dusko, J. Manalo, A. Lucan-Mayer, A. Badolato, I. Ozfidan, L. Gaudreau, S. Studenikin, and A. Sachrajda for discussions. L.S., M.C., M.B., and P.H. acknowledge support from NSERC Discovery and QC2DM Strategic Project Grants as well as the uOttawa Research Chair in Quantum Theory of Materials, Nanostructures and Devices. M.B. acknowledges financial support from the National Science Center (NCN), Poland, Grant Maestro No. 2014/14/A/ST3/00654. M.C. acknowledges support from the Humboldt Foundation. Computing resources from Compute Canada are gratefully acknowledged.

[1] G. F. Giuliani and G. Vignale, *Quantum Theory of the Electron Liquid* (Cambridge University Press, New York, 2005).
[2] C. Attaccalite, S. Moroni, P. Gori-Giorgi, and G. B. Bachelet, Correlation Energy and Spin Polarization in the 2D Electron Gas, Phys. Rev. Lett. **88**, 256601 (2002).
[3] M. Zarenia, D. Neilson, B. Partoens, and F. M. Peeters, Wigner crystallization in transition metal dichalcogenides: A new approach to correlation energy, Phys. Rev. B **95**, 115438 (2017).
[4] S. Sorella and E. Tosatti, Semi-metal-insulator transition of the Hubbard model in the Honeycomb lattice, Europhys. Lett. **19**, 699 (1992).
[5] Y. Otsuka, S. Yunoki, and S. Sorella, Universal Quantum Criticality in the Metal-Insulator Transition of Two-Dimensional Interacting Dirac Electrons, Phys. Rev. X **6**, 011029 (2016).
[6] T. O. Wehling, E. Şaşıoğlu, C. Friedrich, A. I. Lichtenstein, M. I. Katsnelson, and S. Blügel, Strength of Effective Coulomb Interactions in Graphene and Graphite, Phys. Rev. Lett. **106**, 236805 (2011).
[7] A. Lucan, G. Li, A. Reina, J. Kong, R. R. Nair, K. S. Novoselov, A. K. Geim, and E. Y. Andrei, Single-Layer Behavior and Its Breakdown in Twisted Graphene Layers, Phys. Rev. Lett. **106**, 126802 (2011).
[8] Y. Cao, V. Fatemi, A. Demir, S. Fang, S. L. Tomarken, J. Y. Luo, J. D. Sanchez-Yamagishi, K. Watanabe, T. Taniguchi, E. Kaxiras, R. C. Ashoori, and P. Jarillo-Herrero, Correlated insulator behavior at half-filling in magic-angle graphene superlattices, Nature (London) **556**, 80 (2018).
[9] Y. Cao, V. Fatemi, S. Fang, K. Watanabe, T. Taniguchi, E. Kaxiras, and P. Jarillo-Herrero, Unconventional superconductivity in magic-angle graphene superlattices, Nature (London) **556**, 43 (2018).
[10] K. Nomura and A. H. MacDonald, Quantum Hall Ferromagnetism in Graphene, Phys. Rev. Lett. **96**, 256602 (2006).
[11] R. T. Weitz, M. T. Allen, B. E. Feldman, J. Martin, and A. Yacoby, Broken-symmetry states in doubly gated suspended bilayer graphene, Science **330**, 812 (2010).
[12] J. G. Roch, G. Froehlicher, N. Leisgang, P. Makk, K. Watanabe, T. Taniguchi, and R. J. Warburton, Spin-polarized electrons in monolayer MoS2, Nat. Nanotechnol. **14**, 432 (2019).
[13] T. Scrace, Y. Tsai, B. Barman, L. Schweidenback, A. Petrou, G. Kioseoglou, I. Ozfidan, M. Korkusinski, and P. Hawrylak, Magnetoluminescence and valley polarized state of a two-dimensional electron gas in WS2 monolayers, Nat. Nanotechnol. **10**, 603 (2015).
[14] A. K. Geim and I. V. Grigorieva, Van der Waals heterostructures, Nature (London) **499**, 419 (2013).
[15] A. Splendiani, L. Sun, Y. Zhang, T. Li, J. Kim, C.-Y. Chim, G. Galli, and F. Wang, Emerging Photoluminescence in Monolayer MoS_2, Nano Lett. **10**, 1271 (2010).
[16] K. F. Mak, C. Lee, J. Hone, J. Shan, and T. F. Heinz, Atomically Thin MoS_2: A New Direct-Gap Semiconductor, Phys. Rev. Lett. **105**, 136805 (2010).
[17] E. S. Kadantsev and P. Hawrylak, Electronic structure of a single MoS_2 monolayer, Solid State Commun. **152**, 909 (2012).

[18] J. Klinovaja and D. Loss, Spintronics in MoS_2 monolayer quantum wires, Phys. Rev. B **88**, 075404 (2013).

[19] Y. Yu, J. Dang, C. Qian, S. Sun, K. Peng, X. Xie, S. Wu, F. Song, J. Yang, S. Xiao, L. Yang, Y. Wang, X. Shan, M. A. Rafiq, B.-B. Li, and X. Xu, Many-body effect of mesoscopic localized states in MoS_2 monolayer, Phys. Rev. Materials **3**, 051001 (2019).

[20] D. Van Tuan, M. Yang, and H. Dery, Coulomb interaction in monolayer transition-metal dichalcogenides, Phys. Rev. B **98**, 125308 (2018).

[21] C. Volk, S. Fringes, B. Terrés, J. Dauber, S. Engels, S. Trellenkamp, and C. Stampfer, Electronic excited states in bilayer graphene double quantum dots, Nano Lett. **11**, 3581 (2011).

[22] G.-B. Liu, H. Pang, Y. Yao, and W. Yao, Intervalley coupling by quantum dot confinement potentials in monolayer transition metal dichalcogenides, New J. Phys. **16**, 105011 (2014).

[23] A. Kormányos, V. Zólyomi, N. D. Drummond, and G. Burkard, Spin-Orbit Coupling, Quantum Dots, and Qubits in Monolayer Transition Metal Dichalcogenides, Phys. Rev. X **4**, 011034 (2014).

[24] A. D. Güçlü, P. Potasz, M. Korkusinski, and P. Hawrylak, *Graphene Quantum Dots* (Springer-Verlag, Berlin, Heidelberg, 2014).

[25] X.-X. Song, D. Liu, V. Mosallanejad, J. You, T.-Y. Han, D.-T. Chen, H.-O. Li, G. Cao, M. Xiao, G.-C. Guo, and G.-P. Guo, A gate defined quantum dot on the two-dimensional transition metal dichalcogenide semiconductor WSe_2, Nanoscale **7**, 16867 (2015).

[26] J. Pawłowski, D. Żebrowski, and S. Bednarek, Valley qubit in a gated MoS_2 monolayer quantum dot, Phys. Rev. B **97**, 155412 (2018).

[27] R. Pisoni, Z. Lei, P. Back, M. Eich, H. Overweg, Y. Lee, K. Watanabe, T. Taniguchi, T. Ihn, and K. Ensslin, Gate-tunable quantum dot in a high quality single layer MoS_2 van der Waals heterostructure, Appl. Phys. Lett. **112**, 123101 (2018).

[28] S. Bhandari, K. Wang, K. Watanabe, T. Taniguchi, P. Kim, and R. M. Westervelt, Imaging quantum dot formation in MoS_2 nanostructures, Nanotechnology **29**, 42LT03 (2018).

[29] K. Wang, K. De Greve, L. A. Jauregui, A. Sushko, A. High, Y. Zhou, G. Scuri, T. Taniguchi, K. Watanabe, M. D. Lukin, H. Park, and P. Kim, Electrical control of charged carriers and excitons in atomically thin materials, Nat. Nanotechnol. **13**, 128 (2018).

[30] Q. Chen, L. L. Li, and F. M. Peeters, Magnetic field dependence of electronic properties of MoS_2 quantum dots with different edges, Phys. Rev. B **97**, 085437 (2018).

[31] J. Pawłowski, Spin-valley system in a gated MoS_2 - monolayer quantum dot, New J. Phys. **21**, 123029 (2019).

[32] A. Kurzmann, M. Eich, H. Overweg, M. Mangold, F. Herman, P. Rickhaus, R. Pisoni, Y. Lee, R. Garreis, C. Tong, K. Watanabe, T. Taniguchi, K. Ensslin, and T. Ihn, Excited States in Bilayer Graphene Quantum Dots, Phys. Rev. Lett. **123**, 026803 (2019).

[33] T. N. Lin, S. R. M. Santiago, S. P. Caigas, C. T. Yuan, T. Y. Lin, J. L. Shen, and Y. F. Chen, Many-body effects in doped WS2 monolayer quantum disks at room temperature, npj 2D Mater. Appl. **3**, 46 (2019).

[34] M. Bieniek, L. Szulakowska, and P. Hawrylak, Effect of valley, spin, and band nesting on the electronic properties of gated quantum dots in a single layer of transition metal dichalcogenides, Phys. Rev. B **101**, 035401 (2020).

[35] A. Knothe and V. Fal'ko, Quartet states in two-electron quantum dots in bilayer graphene, Phys. Rev. B **101**, 235423 (2020).

[36] D. Y. Qiu, T. Cao, and S. G. Louie, Nonanalyticity, Valley Quantum Phases, and Lightlike Exciton Dispersion in Monolayer Transition Metal Dichalcogenides: Theory and First-Principles Calculations, Phys. Rev. Lett. **115**, 176801 (2015).

[37] J. Jadczak, A. Delgado, L. Bryja, Y. S. Huang, and P. Hawrylak, Robust high-temperature trion emission in monolayers of $Mo(S_ySe_{1-y})_2$ alloys, Phys. Rev. B **95**, 195427 (2017).

[38] M. Bieniek, L. Szulakowska, and P. Hawrylak, Band nesting and exciton spectrum in monolayer MoS_2, Phys. Rev. B **101**, 125423 (2020).

[39] M. Korkusinski, W. Sheng, and P. Hawrylak, Designing quantum systems in self-assembled quantum dots, Phys. Status Solidi B **238**, 246 (2003).

[40] P. Hawrylak, Single-Electron Capacitance Spectroscopy of Few-Electron Artificial Atoms in a Magnetic Field: Theory and Experiment, Phys. Rev. Lett. **71**, 3347 (1993).

[41] S. A. Mikhailov, Quantum-dot lithium in zero magnetic field: Electronic properties, thermodynamics, and Fermi liquid–Wigner solid crossover in the ground state, Phys. Rev. B **65**, 115312 (2002).

[42] M. Korkusiński, P. Hawrylak, M. Ciorga, M. Pioro-Ladrière, and A. S. Sachrajda, Pairing of Spin Excitations in Lateral Quantum Dots, Phys. Rev. Lett. **93**, 206806 (2004).

[43] S. Raymond, S. Studenikin, A. Sachrajda, Z. Wasilewski, S. J. Cheng, W. Sheng, P. Hawrylak, A. Babinski, M. Potemski, G. Ortner, and M. Bayer, Excitonic Energy Shell Structure of Self-Assembled InGaAs/GaAs Quantum Dots, Phys. Rev. Lett. **92**, 187402 (2004).

[44] N. S. Rytova, The screened potential of a point charge in a thin film, Moscow University Physics Bulletin **3**, 18 (1967).

[45] L. Keldysh, Coulomb interaction in thin semiconductor and semimetal films, Sov. J. Exp. Theor. Phys. Lett. **29**, 658 (1979).

[46] F. Wu, F. Qu, and A. H. MacDonald, Exciton band structure of monolayer MoS_2, Phys. Rev. B **91**, 075310 (2015).

[47] A. Wojs and P. Hawrylak, Charging and infrared spectroscopy of self-assembled quantum dots in a magnetic field, Phys. Rev. B **53**, 10841 (1996).

[48] P. Hawrylak, C. Gould, A. Sachrajda, Y. Feng, and Z. Wasilewski, Collapse of the Zeeman gap in quantum dots due to electronic correlations, Phys. Rev. B **59**, 2801 (1999).